



Pollen-based reconstructions of Holocene climate trends in the eastern Mediterranean region

Esmeralda Cruz-Silva^{1,*}, Sandy P. Harrison¹, I. Colin Prentice², Elena Marinova³, Patrick J. Bartlein⁴, Hans Renssen⁵, Yurui Zhang⁶

1: School of Archaeology, Geography & Environmental Science, Reading University, Whiteknights, Reading, RG6 6AH, UK

2: Georgina Mace Centre for the Living Planet, Department of Life Sciences, Imperial College London, Silwood Park Campus, Buckhurst Road, Ascot SL5 7PY, UK

3: Laboratory for Archaeobotany, Baden-Württemberg State Office for Cultural Heritage Management, Fischersteig 9, 78343 Hemmenhofen-Gaienhofen, Germany

4: Department of Geography, University of Oregon, Eugene, Oregon 97403-1251 USA

5: Department of Natural Sciences and Environmental Health, University of South-Eastern Norway, Bø, Norway

6: State Key Laboratory of Marine Environmental Science, College of Ocean & Earth Sciences, Xiamen University, Xiamen, China

*: Corresponding author

1 Abstract

2 There has been considerable debate about the degree to which climate has driven societal changes in the
3 eastern Mediterranean region, partly through reliance on a limited number of qualitative records of climate
4 changes and partly reflecting the need to disentangle the joint impact of changes in different aspects of
5 climate. Here, we use tolerance-weighted Weighted Averaging Partial Least Squares to derive reconstructions
6 of mean temperature of the coldest month (MTCO), mean temperature of the warmest month (MTWA),
7 growing degree days above a threshold of 0°C (GDD0) and plant-available moisture, represented by the ratio
8 of modelled actual to equilibrium evapotranspiration (α) and corrected for past CO₂ changes for 71 individual
9 pollen records from the Eastern Mediterranean region covering part or all of the interval from 12.3 ka to the
10 present. We use these reconstructions to create regional composites that illustrate the long-term trends in
11 each variable. We compare these composites with transient climate model simulations to explore potential
12 causes of the observed trends. We show that the glacial-Holocene transition and the early part of the Holocene
13 was characterised by conditions colder and drier than present. Rapid increases in temperature and moisture
14 occurred between ca 10.3 and 9.3 ka, considerably after the end of the Younger Dryas. Although the time
15 series are characterised by centennial-to-millennial oscillations, MTCO showed a gradual increase from 9 ka
16 to the present, consistent with the expectation that winter temperatures were forced by orbitally-induced
17 increases in insolation during the Holocene. MTWA also showed an increasing trend from 9 ka and reached a
18 maximum of ca 1.5°C greater than present at ca 5 ka, followed by a gradual decline towards present-day
19 conditions. A delayed response to summer insolation changes is likely a reflection of the persistence of the
20 Laurentide and Fennoscandian ice sheets; subsequent summer cooling is consistent with the expected
21 response to insolation changes. Plant-available moisture increased rapidly between 11 and 9.3 ka and
22 conditions were slightly wetter than today between 9-8 ka, but thereafter α declined gradually. These trends
23 likely reflect changes in atmospheric circulation and moisture advection into the region, and were probably
24 too small to influence summer temperature through land-surface feedbacks. Differences in the simulated



25 trajectory of α in different models highlight the difficulties in reproducing circulation-driven moisture
26 advection into the eastern Mediterranean.

27 **1. Introduction**

28 The Eastern Mediterranean region is a critical region for examining the long-term interactions between climate
29 and past societies because of the early adoption of agriculture in the region, which has been widely associated
30 with the rapid warming at the end of the Younger Dryas (Belfer-Cohen and Goring-Morris, 2011). Societal
31 collapse and large-scale migrations have been associated with climates less favourable to agriculture during
32 the 8.2 ka event (Weninger et al., 2006) or to major changes in agricultural practices (Roffet-Salque et al.,
33 2018). Subsequent periods of less favourable climate, particularly prolonged droughts, have been associated
34 with the fall of the Akkadian empire ca. 4.2 ka (Cookson et al., 2019), and the end of the Late Bronze Age and
35 the beginning of the Greek Dark Ages ca 3.2 ka (Kaniewski et al., 2013; Drake, 2012). However, the attribution
36 of changes in human society to climate changes is not universally accepted. Flohr et al. (2016), for example,
37 analysed radiocarbon-dated archaeological sites for evidence of societal changes in response to climate
38 changes in the early Holocene, particularly the 8.2 ka event, and found no evidence of large-scale site
39 abandonment or migration although there were indications of local adaptations. However, since Flohr et al.
40 (2016) did not compare the archaeological records to region-specific climate reconstructions, it is difficult to
41 assess how far local responses might reflect differences in climate between the sites. Even the societal
42 response to the early Holocene warming appears to have differed across the region (Roberts et al., 2018).

43 The need to understand the interactions between climate and past societies in the Eastern Mediterranean is
44 given further impetus because human modification of the landscape has the potential to affect climate directly
45 through changes in land-surface properties. The degree to which human modifications of the landscape had a
46 significant impact on global climate before the pre-industrial period is debated (Ruddiman, 2003; Joos et al.,
47 2004; Kaplan et al., 2011; Singarayer et al., 2011; Mitchell et al., 2013; Stocker et al., 2017), but these impacts
48 were likely to be more important in regions with a long history of settlement and agricultural activities
49 (Harrison et al., 2020).

50 Much of our current understanding of climate changes in the Eastern Mediterranean region is based on the
51 qualitative interpretation of individual records (e.g. Roberts et al., 2019). Oxygen-isotope records from
52 speleothems or lake sediments have been used to infer changes in moisture availability through the Holocene
53 (e.g. Bar-Matthews et al., 1997; Cheng et al., 2015; Dean et al., 2015; Burstyn et al., 2019) as have pollen-
54 based reconstructions of changes in vegetation (e.g. Bottema, 1995; Denèfle et al., 2000; Sadori et al., 2011).
55 Pollen records can also be used to make quantitative reconstructions of seasonal temperatures, and
56 precipitation or plant-available water (Bartlein et al., 2011; Chevalier et al., 2020). Quantitative
57 reconstructions of past climates have been made for individual records from the Eastern Mediterranean
58 region (e.g. Cheddadi and Khater, 2016; Magyari et al., 2019), and syntheses of pollen-based quantitative
59 climate reconstructions have included sites from this region (Davis et al., 2003; Mauri et al., 2015; Herzschuh
60 et al., 2022). Davis et al. (2003) provided a composite curve of seasonal temperature changes, but not moisture
61 changes; both summer and winter temperatures showed very little variation ($<1^{\circ}\text{C}$) through most of the
62 Holocene. Mauri et al. (2015) is an updated version of the Davis et al. (2003) reconstructions, with more sites
63 included but showing similarly muted temperate changes in the Eastern Mediterranean region. Herzschuh et
64 al. (2022) showed more homogenous changes in both temperature and precipitation across the Eastern
65 Mediterranean region but it is difficult to compare the two reconstructions directly because they used
66 different reconstruction techniques. None of the existing reconstructions take account of the impact of



67 changing CO₂ levels on vegetation which could potentially affect the reconstructions of moisture variables
68 (Prentice et al., 2022). Thus, there is a need for well-founded reconstructions of climate, particularly climate
69 variables that are relevant for human occupation and agriculture, to be able to address questions about the
70 interactions between climate and society in the Eastern Mediterranean region.

71 Here, we provide new quantitative reconstructions of seasonal temperature and plant-available moisture for
72 71 sites from the Eastern Mediterranean region (20°E – 62°E, 29°N – 49°N), including a correction for the
73 impact of changing CO₂ levels on plant-available moisture reconstructions. We use these reconstructions to
74 document the regional trends in climate from 12.3 ka to the present. We then explore how far these trends
75 can be explained by changes in external forcing by comparing the reconstructions with transient climate model
76 simulations.

77

78 **2. Methods**

79 **2.1. Modern pollen and climate data**

80 The modern pollen dataset was obtained from version 1 of the SPECIAL Modern Pollen Data Set (SMPDSv1,
81 Harrison, 2019), which provides relative abundance data from 6459 terrestrial sites from Europe, the Middle
82 East and northern Eurasia, assembled from multiple public sources or provided by the original authors. The
83 SMPDS pollen records have been taxonomically standardized, filtered to remove obligate aquatics,
84 insectivorous species, introduced species, or taxa that only occur in cultivation, and to group taxa with only
85 sporadic occurrences into higher taxonomic levels (genus, sub-family or family) and consequently provides
86 relative abundance data for 247 pollen taxa (Supplementary Table 1). We used the 5840 SMPDS sites from the
87 area between 20°W to 62°E and 29°N and 75°N to construct the training data set (Supplementary Figure 1);
88 the sampling outside this box is limited and likely not representative of the diversity of the climate gradients.
89 At sites with multiple modern samples, we averaged the taxon abundances across all samples, to minimise
90 over-representation of some localities and hence specific climates, in the training dataset. We used the 195
91 pollen taxa that occurred at more than 10 sites (Supplementary Table 1) to derive climate-abundance
92 relationships.

93 We focus on reconstructing bioclimatic variables that fundamentally control plant distribution, specifically
94 related to winter temperature limits, accumulated summer warmth and plant-available moisture (Harrison et
95 al., 2010). The bioclimatic data for each modern site was obtained from Harrison et al. (2019), a dataset that
96 provides estimates of mean temperature of the coldest month (MTCO), growing degree days above a base
97 level of 0°C (GDD0), and a moisture index (MI) defined as the ratio of annual precipitation to annual potential
98 evapotranspiration at each modern pollen site, derived using a geographically-weighted regression of version
99 2.0 of the Climate Research Unit (CRU) long-term gridded climatology at 10 arc minute resolution (CRU CL
100 v2.0; New et al., 2002). MTCO and GDD0 were taken directly from the data set. Since Harrison et al. (2019) do
101 not provide mean temperature of the warmest month (MTWA), we calculated this based on the relationship
102 between MTCO and GDD0 given in Wei et al. (2021). We derived an alternative moisture index, α , which is the
103 ratio between modelled actual and equilibrium evapotranspiration, from MI following Liu et al. (2020). MI and
104 α both provide good indices of plant-available moisture, but since α has a natural limit in wetter conditions it
105 is more suitable for discriminating differences in drier climates.



106 2.2. Fossil pollen data

107 The fossil pollen dataset for eastern Mediterranean region was obtained from the Eastern Mediterranean-
108 Black Sea Caspian Corridor (EMBSecBIO) database (Harrison et al., 2021), which contains information from
109 187 records from the region between 29°N and 49°N and 20°E and 62°E. (Note this is a more limited region
110 than used for the modern training data set.) We discarded records (a) from marine environments or very large
111 lakes (>500 km²), (b) with no radiocarbon dating, (c) where the age of the youngest pollen sample was
112 unknown, (d) where there is a hiatus after the youngest radiocarbon date, (e) where more than half of the
113 radiocarbon dates were rejected by the original authors, and (f) where more than half of the ages were based
114 on pollen correlation with other radiocarbon-dated records. However, we kept records where there is a
115 hiatus but where there are sufficient radiocarbon dates above the hiatus to create an age model for the post-
116 hiatus part of the record. We constructed new age models for all the remaining sites (121) using the IntCal20
117 calibration curve (Reimer et al., 2020) and the 'rbacon' R package (Blaauw et al., 2021) in the framework of
118 the 'AgeR' R package (Villegas-Diaz et al., 2021). Some of these records have no modern samples, where
119 modern was defined as 0-300 yr BP, and thus could not be used to calculate climate anomalies. As a result, 71
120 pollen records (Figure 1; Supplementary Table 2) were used for the climate reconstructions. These records
121 have a mean length of 6594 and a mean resolution of 228 years. The records were taxonomically standardized
122 for consistency with the training dataset.

123 2.3 Climate reconstructions

124 We used tolerance-weighted Weighted Averaging Partial Least Squares (*fxTWA-PLS*, Liu et al., 2020) regression
125 to model the relationships between taxon abundances and individual climate variables in the modern training
126 dataset and then applied these relationships to reconstruct past climate using the fossil assemblages. *fxTWA-*
127 *PLS* reduces the known tendency of regression methods to compress climate reconstructions towards the
128 middle of the sampled range by applying a sampling frequency correction to reduce the influence of uneven
129 sampling of climate space, and by weighting the contribution of individual taxa according to their climate
130 tolerance (Liu et al., 2020). Version 2 of *fxTWA-PLS* (*fxTWA-PLS2*, Liu et al., 2023), applied here, uses P-spline
131 smoothing to derive the frequency correction and also applies the correction both in estimating climate
132 optima and in the regression itself, producing a further improvement in model performance relative to version
133 1 as published by Liu et al. (2020).

134 We evaluated the *fxTWA-PLS* models by comparing the reconstructions against observations using pseudo-
135 removed leave-out cross-validation, where one site was randomly selected as a test site and geographically
136 and climatically similar sites (pseudo sites) were removed from the training set to avoid redundancy in the
137 climate information inflating the cross-validation. We selected the last significant component (p -value ≤ 0.01)
138 and assessed model performance using the root mean square error of prediction (RMSEP). The degree of
139 compression was assessed using linear regression and local compression was assessed by loess regression
140 (*locfit*). Climate reconstructions were made for every sample in each fossil record using the best models and
141 sample specific errors were estimated via bootstrapping. We applied a correction factor (Prentice et al., 2022)
142 to the reconstructions of α to account for the impact of changes in atmospheric CO₂ levels on water-use
143 efficiency, which could have impacted the reconstructions during the earliest part of the records. The
144 correction was implemented using the package *codos*: 0.0.2 (Prentice et al., 2022) with past CO₂ concentration
145 values derived from the EPICA Dome C record (Bereiter et al., 2015).



146 **2.4. Construction of climate time series**

147 To obtain climate time series representative of the regional trends in climate, we first screened the
148 reconstructions to remove individual samples with (a) low effective diversity (< 2) as measured using Hill's N_2
149 diversity measure (Hill, 1973), which could indicate low pollen counts or local contamination, and (b) sample-
150 specific errors above the 0.95 quantile to remove obvious outliers. This screening resulted in the exclusion of
151 only a small number of individual samples (see Supplementary Figure 2). We then averaged the reconstructed
152 values in 300-year bins (slightly larger than the average resolution of the records, 228 years) with 50% overlap
153 with the first bin centred on 150 yr BP, and excluding any bins with only one sample. The binned values of
154 individual sites were averaged to produce a regional composite of the anomalies for each climate variable,
155 where the modern baseline was taken as the first 300-yr bin centred on 150 yr BP. These time series were
156 smoothed using locally weighted regression (Cleveland & Devlin, 1988) with a window width of 1000 years
157 (half-window width 500 years) and fixed target points in time to highlight the long-term trends. Confidence
158 intervals (5th and 95th percentiles) for each composite were generated by bootstrap resampling by site over
159 1000 iterations. We examined the impact of the CO₂ correction on reconstructed α (Supplementary Figure 3);
160 this had no major effect on the reconstructed trends except during the earliest part of the record.

161 **2.5. Climate model simulations**

162 We compared the reconstructed climate changes with transient climate model simulations of the response to
163 external forcing, to determine the extent that the reconstructed climate changes reflect changes in known
164 forcing. We used transient simulations of the response to orbital and greenhouse gas forcing in the later
165 Holocene from four models participating in the PAleao-Constraints on Monsoon Evolution and Dynamics
166 (PACMEDY) project (Carré et al., 2021): the MPI (Max Planck Institute) Earth System Model version 1.2
167 (Dallmeyer et al., 2020), the AWI (Alfred Wegener Institute) Earth System Model version 2 (Sidorenko et al.,
168 2019), and two versions of the IPSL (Institut Pierre Simon Laplace) Earth System Model. The IPSL and AWI
169 simulations were run from 6 ka to 1950 CE, the MPI simulation from 7.95 ka to 1850 CE. We used a longer
170 transient simulation covering the period from 11.5 ka made with the LOVECLIM model (Goosse et al., 2010)
171 which, in addition to orbital and greenhouse gas forcing, accounts for the waning of the Laurentide and
172 Fennoscandian ice sheets (Zhang et al., 2016). Finally, we used two transient simulations from 22 ka to present
173 made using the Community Climate System Model (CCSM3; Collins et al., 2006). Both were forced by changes
174 in orbital configuration, atmospheric greenhouse gas concentrations, continental ice sheets and meltwater
175 fluxes, but differ in the configuration meltwater forcing applied after the Bølling warming (14.7 ka). In the first
176 simulation (TRACE-21k-I: Liu et al., 2009), there was a sustained meltwater flux of ~ 0.1 Sv from the Northern
177 Hemisphere ice sheets to the Arctic and North Atlantic until ca 6 ka, and a continuous inflow of water from
178 the North Pacific into the Arctic after the opening of the Bering Strait. The second simulation (TRACE-21k-II;
179 He and Clark, 2022) had no meltwater flux during the Bølling warming or the Holocene but applied a flux of \sim
180 0.17 Sv to the North Atlantic during the Younger Dryas (12.9-11.7 ka). The difference in meltwater forcing
181 results in a much stronger Atlantic Meridional Overturning Circulation during the Holocene in the TRACE-21k-
182 II simulation compared to the TRACE-21k-I simulation. Details of the model simulations are given in
183 Supplementary Table 3. The use of multiple simulations allows the identification of robust signals that are not
184 model-dependent (see e.g. Carré et al., 2021) and also the separation of the effects of different forcings. The
185 TraCE-21k-I data were adjusted to reflect the changing length of months during the Holocene, (related to the
186 eccentricity of Earth's orbit and the precession-determined time of year of perihelion), whereas the other
187 simulations were not. However, this makes little practical difference for the selection of variables used here
188 (Supplementary Figure 4).



189 Outputs from each simulation were extracted for the EMBSecBIO domain (20°W – 55°W, 29°N – 49°N). MTCO
190 and MTWA were extracted directly; GDD0 was obtained by deriving daily temperature values from monthly
191 data using a mean-preserving autoregressive interpolation function (Rymes & Myers, 2001). Daily values of
192 cloud cover fraction and precipitation were obtained from monthly data in the same way, and used to estimate
193 MI through the R package *smpds* (Villegas-Diaz & Harrison, 2022) before converting this to α following Liu et
194 al. (2020). For consistency with the reconstructed time series, climate anomalies for 30-yr bins for each land
195 grid cell within the EMBSecBIO domain were calculated using the interval after 300 yr BP as the modern
196 baseline. Since the resolution of the models varies (Supplementary Table 3), and in any case is coarser than
197 the sampling resolution of the individual pollen records precluding direct comparisons except at a regional
198 scale, we used all of the grid cells within the EMBSecBIO domain and did not attempt to select grid cells
199 coincident with the location of pollen data. A composite was produced by averaging the grid cell time series,
200 which was then smoothed using locally weighted regression (Cleveland & Devlin, 1988) with a window width
201 of 1000 years (i.e. a half-window width of 500 years) and fixed target points in time. Confidence intervals (5th
202 and 95th percentiles) for each composite were generated by bootstrap resampling by grid cell over 1000
203 iterations.

204 **3. Results**

205 **3.1. Model performance**

206 The assessment of the model through cross-validation showed that it reproduces the modern climate variables
207 reasonably well (Table 1, Supplementary Table 4). The best performance is achieved by α ($R^2 = 0.73$, RMSEP =
208 0.15) and MTCO ($R^2 = 0.73$, RMSEP 3.7°). The models for GDD0 ($R^2 = 0.69$, RMSEP = 880) and MTWA ($R^2 = 0.63$,
209 RMSEP = 3.22) were also acceptable. The slopes of the regressions ranged from 0.78 (MTWA) to 0.86 (MTCO),
210 indicating a small degree of compression in the reconstructions (Table 1).

211 **3.2. Holocene climate evolution in the region**

212 Down-core reconstructions showed broadly coherent signals, although there was variation in both the timing
213 and magnitude of climate changes across the sites, reflecting differences in latitude and elevation (Figures 2,
214 3, 4). Nevertheless, the records indicated coherent regional trends over the past 12 ky.

215 Winter temperature showed a cooling trend between 12.3 and 11ka, with reconstructed MTCO ca 8°C lower
216 than present at 11 ka (Figure 5). There was a moderate increase in MTCO after 11 ka, followed by a more
217 pronounced increase of ca 5°C between 10.3 and 9.3 ka. Winter temperatures were only ca 2°C lower than
218 present at the end of this rapid warming phase. MTCO continued to increase gradually through the Holocene,
219 although multi-centennial to millennial oscillations were superimposed on the general trend.

220 The initial trends in summer temperature were broadly similar to those in MTCO, with a cooling between 12.3
221 and 11ka and reconstructed MTWA ca 2°C lower than present at 11 ka (Figure 5). Summer temperature
222 increased thereafter, albeit with pronounced millennial oscillations, up to ca 5 ka when MTWA was ca 1.5°C
223 higher than present. There was a gradual decrease in summer temperature after 5 ka. The GDD0
224 reconstructions showed similar trends to MTWA, reaching maximum values around 5 ka when the growing
225 season was ca 150 degree days greater than today. The subsequent decline in GDD0 was somewhat flatter,
226 which presumably reflects the influence of still-increasing winter temperatures on the length of the growing
227 season.

228 The trends in α differ from the trends in temperature. The driest conditions occur around 11 ka, when α was
229 0.2 less than present (Figure 5), when summer and winter temperatures were also at their lowest. There was



230 a rapid and approximately linear increase in α between 11 and 9.3 ka. Conditions slightly wetter than present
231 (α greater by 0.05–0.075) occurred between 9 and 8 ka. Thereafter there was a gradual and continuous decline
232 in α towards the present. The correction for the physiological impact of low CO_2 prior to 11 ka (Supplementary
233 Figure 3) resulted in drier conditions between 12 and 11 ka than obtained without the correction, and these
234 drier conditions persisted until *ca* 10 ka. The reconstructions with and without the correction are not
235 statistically different between 10 and 5 ka, but the correction produced marginally wetter reconstructions
236 after 5 ka. However, the trend of gradual decline in moisture availability towards the present is not affected
237 by the CO_2 correction.

238 3.3. Comparison with climate simulations

239 The TRACE-21k-I simulation (Figure 6) shows an initial winter warming between 12–11 ka but MTCO is still ca
240 3°C lower than present at 11 ka. There is a gradual increase in MTCO from 11ka onwards, although with
241 centennial-scale variability and a more pronounced oscillation corresponding to the 8.2 ka event. The TRACE-
242 21k-II simulation is initially slightly colder and displays a two-step warming with a peak at 8.5 ka, when MTCO
243 is ca 1.5°C lower than present. The later Holocene trend is similar to that shown in TRACE-21k-I. The LOVECLIM
244 simulation produced generally warmer conditions than either of the TRACE simulations: MTCO is ca 2.5°C
245 lower than present at 11 ka but the two-step warming is more pronounced and peak warming occurs
246 somewhat later at ca 7.5 ka when MTCO was only ca 0.25°C lower than present (Figure 7). While all three
247 models show a rapid warming comparable to the reconstructed warming between 10.3 and 9.3 ka, it is clear
248 that differences in the ice sheet and meltwater forcings affect both the magnitude and the timing of this trend.
249 The overall magnitude of the warming after 9 ka in the TRACE-21k-I simulation is consistent with the
250 reconstructions of MTCO (anomalies of 2.4°C and 2.6°C for model and data respectively). The mid- to late
251 Holocene trend is similar in the PACMEDY simulations (Figure 8) to both TRACE-21k simulations, both in sign
252 and in magnitude (ca 1°C between 6 ka and present) and both are consistent with the reconstructions ($-0.9 \pm$
253 0.7°C). The continuous increase of MTCO is consistent with the change in winter insolation. Given the
254 similarities between the PACMEDY simulations (which only include orbital and greenhouse gas forcing) and
255 the LOVECLIM and TRACE simulations, which also include forcing associated with the relict Laurentide and
256 Fennoscandian ice sheets, it seems likely that orbital forcing was the main driver of winter temperatures in
257 the EMBSecBIO region during the later Holocene.

258 The TRACE-21k-I simulation shows peak summer temperatures between 11–9 ka, when MTWA was ca. 3°C
259 greater than present (Figure 6). The TRACE-21K-II simulations is initially colder than the TRACE-21k-I
260 simulation and the peak in summer temperatures occurs at 9 ka, when MTWA was ca 2.5°C greater than
261 present (Figure 6). The LOVECLIM simulation is warmer than present from 11.5 ka, but peak warming is only
262 reached at 7.5 ka when MTWA is ca 2°C (Figure 7). All three simulations show a gradual decrease in summer
263 temperature through the Holocene after this initial peak. This decreasing trend is also seen in the PACMEDY
264 simulations from 6 ka (or 8 ka in the case of the MPI simulation) onwards (Figure 8) and the magnitude of the
265 change over this interval (ca 2°C from 6ka onwards) is similar to that shown by the TRACE and the LOVECLIM
266 simulations. This similarity suggests that the simulated response is a direct reflection of the change in orbital
267 forcing. However, the reconstructed changes in summer temperature do not show this gradual decline.
268 Reconstructed MTWA is ca 4°C colder than the model predictions at 9 ka. The reconstructions show a gradual
269 increase in MTWA from 9 to 5 ka. Changes in reconstructed temperatures at 5 ka are of a similar magnitude
270 to simulated temperatures at this time (ca 1°C greater than present) although the late Holocene is marked by
271 a cooling trend as seen in the simulations. Thus, while the simulated late Holocene trend is consistent with
272 orbital forcing being the main driver of summer temperatures in the EMBSecBIO region, the early to mid-



273 Holocene trend is not. Previous modelling studies have suggested that the timing of peak warmth differs in
274 different regions of Europe and is associated with the impact of the Fennoscandian ice sheet on regions
275 climates (Renssen et al., 2009; Blascheck and Renssen, 2013; Zhang et al., 2016). The differences in the timing
276 of peak warmth in the EMBSecBIO region in the TRACE-21k-II and LOVECLIM simulations would be consistent
277 with this argument but suggest that the timing and magnitude are model-dependent. It is therefore plausible
278 that the reconstructed trend in MTWA at least during the early Holocene reflects the influence of the relict
279 Laurentide and Fennoscandian ice sheets in modulating the impact of increased summer insolation until the
280 mid-Holocene. Given that GDD₀ is a reflection of both changes in season length, as influenced by winter
281 temperatures, and summer warming, the difference between simulated and reconstructed MTWA are also
282 seen in GDD₀ trends during the early part of the Holocene (Figure 6).

283 The simulations do not show consistent patterns for the trend in α . The TRACE-21k-I simulation (Figure 6)
284 shows a gradual increase, with minor multi-centennial oscillations from 12 ka to present. (Available model
285 output variables are not sufficient to calculate α for the TRACE-21k-II or LOVECLIM simulations). One of the
286 PACMEDY simulations (IPSL-CM5) shows an increase from the mid-Holocene (Figure 8) although the simulated
287 change is an order of magnitude smaller than over the comparable period in the TRACE-21k-I simulation. The
288 AWI model shows no trend in α over this period; the remaining two models show increasing aridity from the
289 mid-Holocene to present (Figure 8). These three models are all broadly consistent with the reconstructions
290 since the reconstructed decrease in α is small. However, the differences in the sign of the trend between the
291 different models indicates that changes in moisture are not a straightforward consequence of the forcing, but
292 must reflect model-dependent changes in moisture supply via changes in atmospheric circulation.
293 Reconstructions of Holocene climates in Iberia have suggested that land-surface feedbacks associated with
294 changes in moisture availability have a strong influence on summer temperature (Liu et al., 2023). There does
295 not seem to be strong evidence for this in the EMBSecBIO region, given the difference in the trends of α and
296 MTWA and the muted nature of the trend in α .

297

298 **4. Discussion**

299 The three temperature-related variables, MTCO, MTWA and GDD₀, all show relatively warm conditions around
300 the late glacial/Holocene transition followed by a cooling that was greatest between *ca* 11 and 10 ka. This
301 pattern is also shown in regional composites (Figure 9) derived from the reconstructions by Mauri et al. (2015)
302 and Herzschuh et al. (2022). However, the magnitude of the cooling shown in the Mauri et al. (2015) and
303 Herzschuh et al. (2022) reconstructions is small compared to our reconstructions. The cool interval starts
304 somewhat later and persists until 9 ka in the Mauri et al. (2015) reconstructions, but this is partly a reflection
305 of the fact that these reconstructions were only made at 1 ka intervals and thus the transitions are less well
306 constrained than in either our reconstructions or those of Herzschuh et al. (2022). This cool interval and the
307 marked warming seen after 10.3 ka in our reconstructions, does not correspond to the Younger Dryas and the
308 subsequent warming. Although the Younger Dryas is considered to be a globally synchronous event (Cheng et
309 al., 2020) and is generally considered coeval with Greenland Stadial I (Larsson et al., 2022), it does not appear
310 to be strongly registered in the EMBSecBIO region in any of the quantitative climate reconstructions. This is
311 consistent with earlier suggestions based on vegetation changes that the Younger Dryas was not a clearly
312 marked feature over much of this region (Bottema, 1995).

313 We have shown that winter temperatures increased sharply between 10.3 and 9.3 ka, but then continued to
314 increase at a more gradual rate through the Holocene. This increasing trend is also seen in the Mauri et al.



315 (2015) reconstructions of MTCO (Figure 9), although the change from the early Holocene to the present is
316 smaller (ca 0.5–1°C) in these reconstructions than in our reconstructions and Mauri et al. (2015) do not show
317 marked cooling around 11 ka. Nevertheless, the consistency between the two reconstructions and between
318 our reconstruction and the simulated changes in MTCO supports the idea that these trends are a response to
319 orbital forcing during the Holocene.

320 Our reconstructions show a gradual increase in summer temperature, as measured by both MTWA and GDD0,
321 from ca 10 to 5 ka when MTWA was ca 1°C warmer than present, followed by a gradual decrease towards the
322 present. This is not consistent with previous reconstructions. Mauri et al. (2015) show an overall increasing
323 trend from 9 ka to present. The Herzschuh et al. (2022) shows a completely different pattern, with the
324 maximum in July temperature at ca. 9 ka and an oscillating but declining trend thereafter (Figure 9). These
325 differences are too large to be caused by differences in the age models applied. They are also unlikely to reflect
326 differences in sampling, since the number of sites used is roughly similar across all three reconstructions (71
327 sites versus 67 sites from Herzschuh et al., 2022 and 409 grid points, based on 57 sites, from Mauri et al.,
328 2015); most sites are common to all three analyses. The differences must therefore be related to the
329 reconstruction method. Herzschuh et al. (2022) used the regression-based approach, Weighted Average
330 Partial Least Squares (WA-PLS), that is the basis for our reconstruction technique, fxtWA-PLSv2. Mauri et al.
331 (2015) used the modern analogue technique. However, after taking account of differences caused by the
332 temporal resolution, there is greater similarity between our reconstructions and those of Mauri et al. (2015)
333 than between either of these reconstructions and the Herzschuh et al. (2022) reconstructions. Several
334 methodological issues could be responsible for the differences between the three sets of reconstructions, and
335 in particular the anomalous moisture trends shown by Herzschuh et al. (2022). Specifically, Herzschuh et al.
336 (2022) used (1) a unique calibration data set for each fossil site based on modern samples within a 2000 km
337 radius of that site, rather than relying on a single training data set; (2) a limited set of 70 dominant taxa rather
338 than the whole pollen assemblage; and (3) included marine records from e.g. the Black Sea, which were
339 excluded in the other reconstructions because they sample an extremely large area and thus are
340 unrepresentative of the local climate.

341 Reconstructed MTWA shows a gradual increase through the early Holocene with maximum values of around
342 1.5°C greater than present reached at ca 5 ka. Previous studies have shown the timing of maximum warmth
343 during the Holocene in Europe varied regionally and the delay compared to the maximum of insolation forcing
344 reflected the impact of the Fennoscandian ice sheet (Renssen et al., 2009; Blascheck and Renssen, 2013; Zhang
345 et al., 2016). Two of the simulations examined here show a delay in the timing of peak warmth, which occurred
346 ca 9 ka in the TRACE-21k-II simulation and ca 7.5 ka in the LOVECLIM simulation. Although both sets of
347 simulations include the relict Laurentide and Fennoscandian ice sheets, neither has realistic ice sheet and
348 meltwater forcing. In the case of the LOVECLIM simulation, for example, the Fennoscandian ice sheet was
349 gone by 10 ka whereas in reality it persisted until at least 8.7 ka (Patton et al., 2017). Thus, the impact of the
350 Fennoscandian ice sheet in delaying orbitally-induced warming could have been greater than shown in this
351 simulation. Nevertheless, the way in which ice sheets and meltwater forcing are implemented varies between
352 models; models are also differentially sensitive to the presence of relict ice sheets (Kapsch et al., 2022). It
353 would be useful to examine the influence of the ice sheets on the climate of the EMBSecBIO region using
354 transient simulations at higher resolution or regional climate models. It has been suggested that meltwater
355 was routed to the Black and Caspian Seas via the Dnieper and Volga Rivers during the early phase of
356 deglaciation (e.g. Yanchilina et al., 2019; Aksu et al. 2022; Vadsaria et al., 2022) and it would also be useful to
357 investigate the impact of this on the regional climate.



358 The availability of water is a crucial factor in the viability of early agriculture (Richerson et al., 2001; Zeder,
359 2011). We have shown that conditions were markedly drier than today (α anomaly ≈ -0.2) around 11 ka but
360 that moisture availability increased to levels only very slightly higher than today (α anomaly $\approx 0.05-0.075$)
361 between 9 and 8 ka, before declining to present-day levels. The initial increase in plant-available water, as
362 indexed by α , could have contributed to promoting the viability of agriculture, as suggested by Richerson et
363 al. (2001). However, subsequent changes are small even at centennial scale (Figure 5). The reconstructed
364 trends in α are not captured in the simulations. Although influenced by temperature-driven changes in
365 evaporation, changes in α in the EMBSecBIO region are likely to be primarily driven by precipitation changes,
366 which in turn are driven by changes in atmospheric circulation. There are indeed large simulated changes in
367 atmospheric circulation through the Holocene in e.g. the LOVECLIM simulations (Supplementary Figure 5) but,
368 as pointed out earlier, differences in the trend of moisture availability between the models imply that the
369 nature of the changes in circulation varies between models and thus does not provide a strong basis for
370 explaining the observed patterns of change in moisture availability. Furthermore, earlier studies, focusing on
371 the western Mediterranean (Liu et al., 2023), Europe (Mauri et al., 2014) and central Eurasia (Bartlein et al.,
372 2017), have shown that models have difficulty in simulating the enhanced moisture transport into the Eurasian
373 continent shown by palaeoenvironmental data during the mid-Holocene and during the late Holocene. Liu et
374 al. (2023) have argued that enhanced moisture transport into the Iberian peninsula during the mid-Holocene
375 led to more vegetation cover and increased evapotranspiration and had a significant impact in reducing
376 growing season temperatures. However, the differences in the trends of summer temperature and plant-
377 available moisture through the Holocene suggests that this land-surface feedback was not an important factor
378 influencing summer temperatures in the EMBSecBIO region.

379 We have focused on the composite picture of regional changes across the EMBSecBIO region, in order to
380 investigate whether these changes could be explained as a consequence of known changes in forcing. The
381 data set also provides information on the trends in climate at individual sites. These data could be used to
382 address the question of whether population density or cultural changes reflect shifts in climate (e.g. Weninger
383 et al., 2006; Drake, 2012; Kaniewski et al., 2013; Cookson et al., 2019; Weiberg et al., 2019; Palmisano et al.,
384 2021). In addition, it would also be possible to use these data to explore the impact of climate changes on the
385 environment, including the natural resources available for people (Harrison et al., in press).

386

387 5. Conclusions

388 We have reconstructed changes in seasonal temperature and in plant-available moisture from 12.3 ka to the
389 present from 71 sites from the EMBSecBIO domain to examine changes in the regional climate of the eastern
390 Mediterranean region. We show that there are regionally coherent trends in these variables. The large
391 increase in both summer and winter temperatures during the early Holocene considerably post-dates the
392 warming observed elsewhere at the end of the Younger Dryas, supporting the idea that the impact of the
393 Younger Dryas in the EMBSecBIO region was muted. Subsequent changes in winter temperature are
394 consistent with the expected response to insolation changes. The timing of peak summer warming occurred
395 later than expected as a consequence of insolation changes and likely, at least in part, reflects the influence
396 of the relict Laurentide and Fennoscandian ice sheets on the regional climate. Drier-than-present conditions
397 are reconstructed at the beginning of the Holocene, but there is a rapid increase in plant-available moisture
398 between 11 and 9 ka, which could have promoted agricultural crops. However, changes in plant-available
399 water during the middle and late Holocene are small even considering centennial-scale variability.



400

401 **Data availability.**

402 Code for the reconstructions of the climatic variables:

403 https://github.com/esmeraldacs/EMBSeCBIO_Holocene_climate

404 **Author Contributions**

405 ECS, SPH, ICP designed the study; EM, SPH and ECS revised EMBSeCBIO database including the construction
406 of new age models; PJB, HR and YZ provided climate model output; ECS performed the analyses; SPH and ECS
407 wrote the first draft of the paper; all authors contributed to the final version.

408 **Competing Interests**

409 The authors declare there are no competing interests.

410 **Acknowledgements.**

411 We thank members of the SPECIAL team in Reading and from the Leverhulme Centre for Wildfires,
412 Environment and Society for useful discussions about these analyses.

413 **Financial support.**

414 ECS and SPH acknowledge funding support from the ERC-funded project GC2.0 (Global Change 2.0: Unlocking
415 the past for a clearer future, grant number 694481) and from the Leverhulme Centre for Wildfires,
416 Environment and Society through the Leverhulme Trust, grant number RC-2018-023.

417



418 References

- 419 Aksu, A. E., and Hiscott, R. N.: Persistent Holocene outflow from the Black Sea to the eastern Mediterranean
420 Sea still contradicts the Noah's Flood Hypothesis: A review of 1997–2021 evidence and a regional
421 paleoceanographic synthesis for the latest Pleistocene–Holocene, *Earth Sci. Rev.*, 227, 103960,
422 <https://doi.org/10.1016/j.earscirev.2022.103960>, 2022.
- 423 Bar-Matthews, M., Ayalon, A., and Kaufman, A.: Late Quaternary paleoclimate in the eastern Mediterranean
424 region from stable isotope analysis of speleothems at Soreq Cave, Israel, *Quat. Res.*, 47, 155–168,
425 <https://doi.org/10.1006/qres.1997.1883>, 1997.
- 426 Bartlein, P. J., Harrison, S.P., Brewer, S., Connor, S., Davis B.A.S., Gajewski, K., Guiot, J., Harrison-Prentice, T.
427 I., Henderson, A., Peyron, O., Prentice, I. C., Scholze, M., Seppä, H., Shuman, B., Sugita, S., Thompson, R. S.,
428 Viau, A., Williams, J., and Wu, H.: Pollen-based continental climate reconstructions at 6 and 21 ka: a global
429 synthesis, *Clim. Dynam.*, 37, 775–802, 2011.
- 430 Bartlein, P.J., Harrison, S.P., and Izumi, K.: Underlying causes of Eurasian mid-continental aridity in
431 simulations of mid-Holocene climate, *Geophys. Res. Lett.*, 44, 9020–9028, doi: 10.1002/2017GL074476, 2017.
- 432 Belfer-Cohen, A., & Goring-Morris, A. N. Becoming Farmers: The Inside Story. *Current Anthropology*, 52(S4),
433 S209–S220. <https://doi.org/10.1086/658861>, 2011.
- 434 Bereiter, B., Eggleston, S., Schmitt, J., Nehrbass-Ahles, C., Stocker, T.F., Fischer, H., Kipfstuhl, S., and
435 Chappellaz, J.: Revision of the EPICA Dome C CO₂ record from 800 to 600 kyr before present, *Geophys. Res.*
436 *Lett.*, 42, 542–549, <https://doi.org/10.1002/2014GL061957>, 2015.
- 437 Bini, M., Zanchetta, G., Perşoiu, A., Cartier, R., Català, A., Cacho, I., Dean, J.R., Di Rita, F., Drysdale, R.N.,
438 Finnè, M., Isola, I., Jalali, B., Lirer, F., Magri, D., Masi, A., Marks, L., Mercuri, A.M., Peyron, O., Sadori, L., ...
439 and Brisset, E.: The 4.2 ka BP Event in the Mediterranean region: An overview, *Clim. Past*, 15, 555–577,
440 <https://doi.org/10.5194/cp-15-555-2019>, 2019.
- 441 Bird, D., Miranda, L., Vander Linden, M., Robinson, E., Bocinsky, R.K., Nicholson, C., Capriles, J.M., Finley, J.B.,
442 Gayo, E.M., Gil, A., d'Alpoim Guedes, J., Hoggarth, J.A., Kay, A., Loftus, E., Lombardo, U., Mackie, M.,
443 Palmisano, A., Solheim, S., Kelly, R.L., and Freeman, J.: P3k14c, a synthetic global database of archaeological
444 radiocarbon dates, *Sci. Data*, 9, 27, <https://doi.org/10.1038/s41597-022-01118-7>, 2022.
- 445 Blaauw, M., Christen, J.A., Aquino Lopez, M.A., Vazquez, J.E., Gonzalez V.O.M., Belding, T., Theiler, J., Gough,
446 B., and Karney, C.: *rbacon: Age-Depth Modelling using Bayesian Statistics (2.5.6)* [R]. [https://CRAN.R-](https://CRAN.R-project.org/package=rbacon)
447 [project.org/package=rbacon](https://CRAN.R-project.org/package=rbacon), 2021. (last accessed 17 April 2023)
- 448 Blaschek, M., and Renssen, H.: The Holocene thermal maximum in the Nordic Seas: the impact of Greenland
449 Ice Sheet melt and other forcings in a coupled atmosphere-sea-ice-ocean model, *Clim. Past*, 9, 1629–1643,
450 [10.5194/cp-9-1629-2013](https://doi.org/10.5194/cp-9-1629-2013), 2013.
- 451 Bottema, S.: The Younger Dryas in the eastern Mediterranean, *Quat. Sci. Rev.*, 14, 883–891,
452 [https://doi.org/10.1016/0277-3791\(95\)00069-0](https://doi.org/10.1016/0277-3791(95)00069-0), 1995.
- 453 Burstyn, Y., Martrat, B., Lopez, J. F., Iriarte, E., Jacobson, M.J., Lone, M.A., and Deininger, M.: Speleothems
454 from the Middle East: An example of water limited environments in the SISAL database. *Quaternary*, 2, 16.
455 <https://doi.org/10.3390/quat2020016>, 2019.
- 456 Carré, M., Braconnot, P., Elliot, M., d'Agostino, R., Schurer, A., Shi, X., Marti, O., Lohmann, G., Jungclauss, J.,
457 Cheddadi, R., Abdelkader di Carlo, I., Cardich, J., Ochoa, D., Salas Gismondi, R., Pérez, A., Romero, P.E., Turcq,



- 458 B., Corrège, T., and Harrison, S.P.: High-resolution marine data and transient simulations support orbital
459 forcing of ENSO amplitude since the mid-Holocene. *Quat. Sci. Rev.*, 268, 107125.
460 <https://doi.org/10.1016/j.quascirev.2021.107125>, 2021.
- 461 Cheddadi, R., and Khater, C.: Climate change since the last glacial period in Lebanon and the persistence of
462 Mediterranean species, *Quat. Sci. Rev.*, 150, 146-157, <https://doi.org/10.1016/j.quascirev.2016.08.010>,
463 2016.
- 464 Cheng, H., Sinha, A., Verheyden, S., Nader, F.H., Li, X.L., Zhang, P.Z., Yin, J.J., Yi, L., Peng, Y.B., Rao, Z.G., Ning,
465 Y.F., and Edwards, R.L.: The climate variability in northern Levant over the past 20,000 years, *Geophys. Res.*
466 *Let.*, 42, 8641–8650, <https://doi.org/10.1002/2015GL065397>, 2015.
- 467 Cheng, H., Zhang, H., Spötl, C., Baker, J., Sinha, A., Li, H., Bartolomé, M., Moreno, A., Kathayat, G., Zhao, J.,
468 Dong, X., Li, Y., Ning, Y., Jia, X., Zong, B., Ait Brahim, Y., Pérez-Mejías, C., Cai, Y., Novello, V.F., Cruz, F.W.,
469 Severinghaus, J.P., An, Z., and Edwards, R.L.: Timing and structure of the Younger Dryas event and its
470 underlying climate dynamics, *Proc. Natl. Acad. Sci. USA*, 117, 23408-23417, doi: 10.1073/pnas.2007869117,
471 2020.
- 472 Chevalier, M., Davis, B.A.S., Heiri, O., Seppä, H., Chase, B.M., Gajewski, K., Lacourse, T., Telford, R.J.,
473 Finsinger, W., Guiot, J., Kühl, N., Maezumi, S.Y., Tipton, J.R., Carter, V.A., Brussel, T., Phelps, L.N., Dawson, A.,
474 Zanon, M., Vallé, F., Nolan, C., Mauri, A., de Vernal, A., Izumi, K., Holmström, L., Marsicek, J., Goring, S.,
475 Sommer, P.S., Chaput, M., and Kupriyanov, D.: Pollen-based climate reconstruction techniques for late
476 Quaternary studies, *Earth Sci. Rev.*, 210, 103384, <https://doi.org/10.1016/j.earscirev.2020.103384>, 2020.
- 477 Cleveland, W.S., and Devlin, S.J.: Locally weighted regression: An approach to regression analysis by local
478 fitting, *J. Am. Stat. Assoc.*, 83, 596–610. <https://doi.org/10.1080/01621459.1988.10478639>, 1988.
- 479 Cookson, E., Hill, D.J., and Lawrence, D.: Impacts of long term climate change during the collapse of the
480 Akkadian Empire, *J. Arch. Sci.*, 106, 1-9, <https://doi.org/10.1016/j.jas.2019.03.009>, 2019.
- 481 Collins, W.D., Bitz, C.M., Blackmon, M.L., Bonan, G.B., Bretherton, C.S., Carton, J.A., Chang, P., Doney, S.C.,
482 Hack, J.J., Henderson, T.B., Kiehl, J.T., Large, W.G., McKenna, D.S., Santer, B.D., and Smith, R.D.: The
483 Community Climate System Model version 3 (CCSM3), *J. Clim.*, 19, 2122-2143,
484 <http://dx.doi.org/10.1175/JCLI3761.1>, 2006.
- 485
486 Connor, S., Colombaroli, D., Confortini, F., Gobet, E., Ilyashuk, B.P., Ilyashuk, E.A., van Leeuwen, J.F.N.,
487 Lamentowicz, M., van der Knaap, W.O., Malysheva, E., Marchetto, A., Margalitzadze, N., Mazei, Y., Mitchell,
488 E.A.D., Payne, R.J., and Ammann, B.: Long-term population dynamics: Theory and reality in a peatland
489 ecosystem, *J. Ecol.*, 106, 1, <https://doi.org/10.1111/1365-2745.12865>, 2017.
- 490 Cruz-Silva, E., Harrison, S.P., Marinova, E., and Prentice, I.C.: A new method based on surface-sample pollen
491 data for reconstructing palaeovegetation patterns, *J. Biogeog.*, 49, 1381–1396,
492 <https://doi.org/10.1111/jbi.14448>, 2022.
- 493 Dallmeyer, A., Claussen, M., Lorenz, S.J., and Shanahan, T.: The end of the African humid period as seen by a
494 transient comprehensive Earth system model simulation of the last 8000-years, *Clim. Past*, 16, 117–140,
495 <https://doi.org/10.5194/cp-16-117-2020>, 2020.
- 496 Davis, B.A.S., Brewer, S., Stevenson, A.C., and Guiot, J.: The temperature of Europe during the Holocene
497 reconstructed from pollen data, *Quat. Sci. Rev.*, 22: 1701-1716, [https://doi.org/10.1016/S0277-](https://doi.org/10.1016/S0277-3791(03)00173-2)
498 [3791\(03\)00173-2](https://doi.org/10.1016/S0277-3791(03)00173-2), 2003.



- 499 Davis, T.W., Prentice, I.C., Stocker, B.D., Thomas, R.T., Whitley, R.J., Wang, H., Evans, B.J., Gallego-Sala, A.V.,
500 Sykes, M.T., and Cramer, W.: Simple process-led algorithms for simulating habitats (SPLASH v.1.0): Robust
501 indices of radiation, evapotranspiration and plant-available moisture, *Geosci. Model Dev.*, 10, 689–708,
502 <https://doi.org/10.5194/gmd-10-689-2017>, 2017.
- 503 Dean, J.R., Jones, M.D., Leng, M.J., Noble, S.R., Metcalfe, S.E., Sloane, H.J., Sahy, D., Eastwood, W.J., and
504 Roberts, C.N.: Eastern Mediterranean hydroclimate over the late glacial and Holocene, reconstructed from
505 the sediments of Nar lake, central Turkey, using stable isotopes and carbonate mineralogy, *Quat. Sci. Rev.*,
506 124, 162–174, <https://doi.org/10.1016/j.quascirev.2015.07.023>, 2015.
- 507 Denèfle, M., Lézine, A., Fouache, E., and Dufaure, J.: A 12,000-Year pollen record from Lake Maliq,
508 Albania, *Quat. Res.*, 54, 423–432, doi:10.1006/qres.2000.2179, 2000.
- 509 Drake, B.L.: The influence of climatic change on the Late Bronze Age Collapse and the Greek Dark Ages. *J.*
510 *Arch. Sci.*, 39, 1862–1870, <https://doi.org/10.1016/j.jas.2012.01.029>, 2012.
- 511 Flohr, P., Fleitmann, D., Matthews, R., Matthews, W., and Black, S.: Evidence of resilience to past climate
512 change in Southwest Asia: Early farming communities and the 9.2 and 8.2 ka events, *Quat. Sci. Rev.*, 136, 23–
513 39, <https://doi.org/10.1016/j.quascirev.2015.06.022>, 2016.
- 514 Goosse, H., Brovkin, V., Fichefet, T., Haarsma, R., Huybrechts, P., Jongma, J., Mouchet, A., Selten, F., Barriat,
515 P.-Y., Campin, J.-M., Deleersnijder, E., Driesschaert, E., Goelzer, H., Janssens, I., Loutre, M.-F., Morales
516 Maqueda, M. A., Opsteegh, T., Mathieu, P.-P., Munhoven, G., Pettersson, E. J., Renssen, H., Roche, D. M.,
517 Schaeffer, M., Tartinville, B., Timmermann, A., and Weber, S. L.: Description of the Earth system model of
518 intermediate complexity LOVECLIM version 1.2, *Geosci. Model Dev.*, 3, 603–633,
519 <https://doi.org/10.5194/gmd-3-603-2010>, 2010.
- 520 Goring-Morris, A.N., and Belfer-Cohen, A.: Evolving human/animal interactions in the Near Eastern Neolithic:
521 feasting as a case study, In G. Aranda, S. Monton, & M. Sanchez (Eds) *Guess Who's Coming to Dinner.*
522 *Feasting Rituals in the Prehistoric Societies of Europe and Near East*, pp. 64–72, Oxbow Books, Oxford, 2011.
- 523 Harrison, S.P.: Modern pollen data for climate reconstructions, version 1 (SMPDS) [Data set]. University of
524 Reading. <https://doi.org/10.17864/1947.194>, 2019. (last accessed 17 April 2023)
- 525 Harrison, S. P., and Prentice, I.C.: Climate and CO₂ controls on global vegetation distribution at the Last
526 Glacial Maximum: Analysis based on palaeovegetation data, biome modelling and palaeoclimate simulations,
527 *Glob. Change Biol.*, 9, 983–1004, <https://doi.org/10.1046/j.1365-2486.2003.00640.x>, 2003.
- 528 Harrison, S. P., Marinova, E., and Cruz-Silva, E.: EMBSecBIO pollen database [Data set]. University of Reading.
529 <https://doi.org/10.17864/1947.309>, 2021. (last accessed 17 April 2023)
- 530 Harrison, S.P., Prentice, I.C., Sutra J-P., Barboni, D., Kohfeld, K.E. and Ni. J.: Ecophysiological and bioclimatic
531 foundations for a global plant functional classification, *J. Veg. Sci.* 21, 300–317, doi 10.1111/j.1654-
532 1103.2009.01144x, 2010.
- 533 Harrison, S.P., Gaillard, M-J., Stocker, B., Vander Linden, M., Klein Goldewijk, K., Boles, O., Braconnot, P.,
534 Dawson, A., Fluet-Chouinard, E., Kaplan, J.O., Kastner, T., Pausata, F.S.R., Robinson, E., Whitehouse, N.,
535 Madella, M., Morrison, K.D.: Development and testing of scenarios for implementing Holocene LULC in Earth
536 System Model experiments, *Geosci. Model Dev.*, 13, 805–824, <https://doi.org/10.5194/gmd-13-805-2020>,
537 2020.



- 538 Harrison, S.P., Cruz-Silva, E., Haas, O., Liu, M., Parker, S., Qiao, S., Luke Sweeney, L., in press. Tools and
539 approaches to addressing the climate-humans nexus during the Holocene. Proceedings of the 12th ICAANE
540 Congress, Harrassowitz Verlag.
- 541 He, F., and Clark, P.U.: Freshwater forcing of the Atlantic Meridional Overturning Circulation revisited. *Nat.*
542 *Clim. Change*, 12, 449-454, <https://doi.org/10.1038/s41558-022-01328-2>, 2022.
- 543 Hengl, T.: Potential distribution of biomes (Potential Natural Vegetation) at 250 m spatial resolution [data
544 set], <https://doi.org/10.5281/zenodo.3526620>, 2019 (last accessed 17 April 2023)
- 545 Herzschuh, U., Böhmer, T., Li, C., Cao, X., Hébert, R., Dallmeyer, A., Telford, R.J. and Kruse, S.: Reversals in
546 temperature-precipitation correlations in the Northern Hemisphere extratropics during the
547 Holocene, *Geophys. Res. Lett.*, 49, e2022GL099730, <https://doi.org/10.1029/2022GL099730>, 2022.
- 548 Hill, M.O.: Diversity and evenness: A unifying notation and its consequences, *Ecol.* 54, 427–432,
549 <https://doi.org/10.2307/1934352>, 1973.
- 550 Jalut, G., Dedoubat, J.J., Fontugne, M., and Otto, T.: Holocene circum-Mediterranean vegetation changes:
551 Climate forcing and human impact, *Quat. Int.*, 200, 4–18, <https://doi.org/10.1016/j.quaint.2008.03.012>,
552 2009.
- 553 Joos, F., Gerber, S., Prentice, I.C., Otto-Bliesner, B.L., and Valdes, P.J.: Transient simulations of Holocene
554 atmospheric carbon dioxide and terrestrial carbon since the last glacial maximum, *Glob. Biogeochem. Cy.*,
555 18, GB2002, doi:10.1029/2003GB002156, 2004.
- 556 Kaniewski, D., Van Campo, E., Guiot, J., Le Burel, S., Otto, T., and Baeteman, C.: Environmental roots of the
557 Late Bronze Age Crisis. *PLoS ONE*, 8, e71004. <https://doi.org/10.1371/journal.pone.0071004>, 2013.
- 558 Kaplan, J.O., Krumhardt, K.M., Ellis, E.C., Ruddiman, W.F., Lemmen, C., and Klein Goldewijk, K.: Holocene
559 carbon emissions as a result of anthropogenic land cover change, *Holocene*, 21, 775-791, 2011.
- 560 Kapsch, M.-L., Mikolajewicz, U., Ziemen, F., and Schannwell, C.: Ocean response in transient simulations of
561 the last deglaciation dominated by underlying ice-sheet reconstruction and method of meltwater
562 distribution, *Geophys. Res. Lett.*, 49, e2021GL096767, <https://doi.org/10.1029/2021GL096767>, 2022.
- 563 Larsson, S.A., Kylander, M.E., Sannel, A.B.K., and Hammarlund, D.: Synchronous or not? The timing of the
564 Younger Dryas and Greenland Stadial-1 reviewed using tephrochronology. *Quaternary*, 5, 19,
565 <https://doi.org/10.3390/quat5020019>, 2022.
- 566 Liu, M., Prentice, I.C., ter Braak, C.J.F., and Harrison, S.P.: An improved statistical approach for reconstructing
567 past climates from biotic assemblages, *Proc. Roy. Soc. A: Math., Phy. Eng. Sci.*, 476, 20200346.
568 <https://doi.org/10.1098/rspa.2020.0346>, 2020.
- 569 Liu, M., Shen, Y., González-Sampérez, P., Gil-Romera, G., ter Braak, C.J.F. Prentice, I.C., and Harrison, S.P.:
570 Holocene climates of the Iberian Peninsula, *Clim. Past*, 19, 803-834, [https://doi.org/10.5194/cp-19-803-](https://doi.org/10.5194/cp-19-803-2023)
571 [2023](https://doi.org/10.5194/cp-19-803-2023), 2023.
- 572 Liu, Z., Otto-Bliesner, B. L., He, F., Brady, E. C., Tomas, R., Clark, P. U., Carlson, A. E., Lynch-Stieglitz, J., Curry,
573 W., Brook, E., Erickson, D., Jacob, R., Kutzbach, J., and Cheng, J.: Transient Simulation of Last Deglaciation
574 with a New Mechanism for Bolling-Allerod Warming, *Science*, 325, 310-314,
575 doi:10.1126/science.1171041, 2009.
576



- 577 Magyari, E.K., Pál, I., Vincze, I., Veres, D., Jakab, G., Braun, M., Szalai, Z., Szabó, Z., and Korponai, J.: Warm
578 Younger Dryas summers and early late glacial spread of temperate deciduous trees in the Pannonian Basin
579 during the last glacial termination (20-9 kyr cal BP), *Quat. Sci. Rev.*, 225, 105980,
580 doi.org/10.1016/j.quascirev.2019.105980, 2019.
- 581 Marinova, E., Harrison, S.P., Bragg, F., Connor, S., de Laet, V., Leroy, S.A.G., Mudie, P., Atanassova, J.,
582 Bozilova, E., Caner, H., Cordova, C., Djamali, M., Filipova-Marinova, M., Gerasimenko, N., Jahns, S., Kouli, K.,
583 Kotthoff, U., Kvavadze, E., Lazarova, M., ... and Tonkov, S.: Pollen-derived biomes in the Eastern
584 Mediterranean–Black Sea–Caspian–Corridor, *J. Biogeog.*, 45, 484–499, <https://doi.org/10.1111/jbi.13128>,
585 2018.
- 586 Martin Calvo, M., and Prentice, I.C.: Effects of fire and CO₂ on biogeography and primary production in glacial
587 and modern climates, *New Phytol.*, 208, 987–994. <https://doi.org/10.1111/nph.13485>, 2015.
- 588 Mauri, A., Davis, B.A.S., Collins, P.M., and Kaplan, J.O.: The influence of atmospheric circulation on the mid-
589 Holocene climate of Europe: a data–model comparison, *Clim. Past*, 10, 1925–1938,
590 <https://doi.org/10.5194/cp-10-1925-2014>, 2014.
- 591 Mauri, A., Davis, B.A.S., Collins, P.M., Kaplan, J.O.: The climate of Europe during the Holocene: a gridded
592 pollen-based reconstruction and its multi-proxy evaluation, *Quat. Sci. Rev.*, 112, 109-127,
593 <https://doi.org/10.1016/j.quascirev.2015.01.013>, 2015.
- 594 Messenger, E., Belmecheri, S., Von Grafenstein, U., Vincent, O., Voinchet, P., Puaud, S., Courtin-nomade, A.,
595 Guillou, H., Mgeladze, A., Dumoulin, J.-P., Mazuy, A., and Lordkipanidze, D.: Late Quaternary record of the
596 vegetation and catchment-related changes from Lake Paravani (Javakheti, South Caucasus), *Quat. Sci. Rev.*,
597 77, 125–140, <https://doi.org/10.1016/j.quascirev.2013.07.011>, 2013.
- 598 Mitchell, L., Brook, E., Lee, J., Buizert, C., and Sowers, T.: Constraints on the late Holocene anthropogenic
599 contribution to the atmospheric methane budget, *Science*, 342, 964–966, doi:10.1126/science.1238920,
600 2013.
- 601 New, M., Lister, D., Hulme, M., and Makin, I.: A high-resolution data set of surface climate over global land
602 areas, *Clim. Res.*, 21, 1–25. <https://doi.org/10.3354/cr021001>, 2002.
- 603 Otto-Bliesner, B.L., Braconnot, P., Harrison, S.P., Lunt, D.J., Abe-Ouchi, A., Albani, S., Bartlein, P.J., Capron, E.,
604 Carlson, A.E., Dutton, A., Fischer, H., Goelzer, H., Govin, A., Haywood, A., Joos, F., LeGrande, A.N., Lipscomb,
605 W.H., Lohmann, G., Mahowald, N., ... and Zhang, Q.: The PMIP4 contribution to CMIP6 – Part 2: Two
606 interglacials, scientific objective and experimental design for Holocene and Last Interglacial simulations,
607 *Geosci. Model Dev.*, 10, 3979–4003. <https://doi.org/10.5194/gmd-10-3979-2017>, 2017.
- 608 Palmisano, A., Bevan, A., Kabelindde, A., Roberts, N., and Shennan, S.: Long-term demographic trends in
609 prehistoric Italy: Climate impacts and regionalised socio-ecological trajectories, *J. World Prehist.*, 34, 381–
610 432, <https://doi.org/10.1007/s10963-021-09159-3>, 2021.
- 611 Patton, H., Hubbard, A., Andreassen, K., Auriac, A., Whitehouse, P.L., Stroeven, A.P., Shackleton, C.,
612 Winsborrow, M., Heyman, J., and Hall, A.M.: Deglaciation of the Eurasian ice sheet complex, *Quat. Sci. Rev.*,
613 169, 148–172, <https://doi.org/10.1016/j.quascirev.2017.05.019>, 2017.
- 614 Prentice, I.C., Harrison, S.P., and Bartlein, P.J.: Global vegetation and terrestrial carbon cycle changes after
615 the last ice age, *New Phytol.* 189, 988–998, <https://doi.org/10.1111/j.1469-8137.2010.03620.x>, 2011.



- 616 Prentice, I.C., Villegas-Díaz, R., and Harrison, S.P.: Accounting for atmospheric carbon dioxide variations in
617 pollen-based reconstruction of past hydroclimates, *Glob. Planet. Change*, 211, 103790.
618 <https://doi.org/10.1016/j.gloplacha.2022.103790>, 2022.
- 619 Prentice, I.C., Villegas-Díaz, R., and Harrison, S.P.: *codos: 0.0.2* (0.0.2). Zenodo.
620 <https://doi.org/10.5281/ZENODO.5083309>, 2022 (last accessed 17 April 2023)
- 621 Reimer, P., Austin, W. E. N., Bard, E., Bayliss, A., Blackwell, P. G., Ramsey, C. B., Butzin, M., Cheng, H.,
622 Edwards, R. L., Friedrich, M., Grootes, P. M., Guilderson, T. P., Hajdas, I., Heaton, T. J., Hogg, A. G., Hughen, K.
623 A., Kromer, B., Manning, S. W., Muscheler, R., ... and Talamo, S.: The IntCal20 Northern Hemisphere
624 radiocarbon age calibration curve (0-55 cal kBP), *Radiocarbon*, 62, 725-757,
625 <https://doi.org/10.1017/RDC.2020.41>, 2020.
- 626 Renssen, H., Seppä, H., Heiri, O., Roche, D.M., Goosse, H., and Fichet, T.: The spatial and temporal
627 complexity of the Holocene thermal maximum, *Nat. Geosci.* 2, 411–414, <https://doi.org/10.1038/ngeo513>,
628 2009.
- 629 Richerson, P.J., Boyd, R., and Bettinger, R.L.: Was agriculture impossible during the Pleistocene but
630 mandatory during the Holocene? A climate change hypothesis, *Am. Antiq.*, 66, 387–411,
631 <https://doi.org/10.2307/2694241>, 2001.
- 632 Roberts, N., Brayshaw, D., Kuzucuoğlu, C., Perez, R., and Sadori, L.: The mid-Holocene climatic transition in
633 the Mediterranean: Causes and consequences, *Holocene*, 21, 3–13,
634 <https://doi.org/10.1177/0959683610388058>, 2011.
- 635 Roberts, N., Cassis, M., Doonan, O., Eastwood, W., Elton, H., Haldon, J., Izdebski, A., and Newhard, J.: Not the
636 End of the World? Post-classical decline and recovery in rural Anatolia, *Hum. Ecol.*, 46, 305–322,
637 <https://doi.org/10.1007/s10745-018-9973-2>, 2018.
- 638 Roberts, C.N., Woodbridge, J., Palmisano, A., Bevan, A., Fyfe, R., and Shennan, S.: Mediterranean landscape
639 change during the Holocene: Synthesis, comparison and regional trends in population, land cover and
640 climate, *Holocene*, 29, 923–937, <https://doi.org/10.1177/0959683619826697>, 2019.
- 641 Roffet-Salque, M., Marciniak, A., Valdes, P.J., Pawłowska, K., Pyzel, J., Czerniak, L., Krüger, M., Roberts, C.N.,
642 Pitter, S., Evershed, R.P.: Evidence for the impact of the 8.2-ky BP climate event on Near Eastern early
643 farmers, *Proc Natl Acad Sci USA*, 115, 8705-8709, doi: 10.1073/pnas.1803607115. 2018.
- 644 Ruddiman, W. F.: The anthropogenic greenhouse era began thousands of years ago, *Clim. Change*, 61, 261–
645 293, doi:10.1023/B:CLIM.0000004577.17928.fa, 2003.
- 646 Rymes, M.D., and Myers, D.R.: Mean preserving algorithm for smoothly interpolating averaged data. *Solar*
647 *Energy*, 71, 225–231, [https://doi.org/10.1016/S0038-092X\(01\)00052-4](https://doi.org/10.1016/S0038-092X(01)00052-4), 2001.
- 648 Sadori, L., Jahns, S., and Peyron, O.: Mid-Holocene vegetation history of the central Mediterranean,
649 *Holocene*, 21, 117-129, <https://doi.org/10.1177/0959683610377530>, 2011.
- 650 Sidorenko, D., Goessling, H. f., von Koldunov, N., Scholz, P., Danilov, S., Barbi, D., Cabos, W., Gurses, O.,
651 Harig, S., Hinrichs, C., Juricke, S., Lohmann, G., Losch, M., Mu, L., Rackow, T., Rakowsky, N., Sein, D.,
652 Semmler, T., Shi, X., ... and Jung, T.: Evaluation of FESOM2.0 coupled to ECHAM6.3: Preindustrial and
653 HighResMIP simulations, *J. Adv. Model. Earth Syst.*, 11, 3794–3815, <https://doi.org/10.1029/2019MS001696>,
654 2019.



- 655 Singarayer, J.S., Valdes, P.J., Friedlingstein, P., Nelson, S., and Beerling, D.J.: Late Holocene methane rise
656 caused by orbitally controlled increase in tropical sources, *Nature*, 470, 82–85, doi:10.1038/nature09739,
657 2011.
- 658 Stocker, B.D., Yu, Z., Massa, C., and Joos, F.: Holocene peatland and ice-core data constraints on the timing
659 and magnitude of CO₂ emissions from past land use, *Proc. Natl. Acad. Sci.*, 114, 1492–1497,
660 doi:10.1073/pnas.1613889114, 2017.
- 661 Vadsaria, T., Zaragosi, S., Ramstein, G., Dutay, J.-C., Li, L., Siani, G., Revel, M., Obase, T., and Abe-Ouchi,
662 A.: Freshwater influx to the Eastern Mediterranean Sea from the melting of the Fennoscandian ice sheet
663 during the last deglaciation, *Sci. Rep.* 12, 8466, <https://doi.org/10.1038/s41598-022-12055-1>, 2022.
- 664 Villegas-Diaz, R., and Harrison, S. P.: The SPECIAL Modern Pollen Data Set for Climate Reconstructions,
665 version 2 (SMPDSv2), University of Reading. Dataset, <https://doi.org/10.17864/1947.000389>, 2022. (last
666 accessed 17 April 2023).
- 667 Villegas-Diaz, R., and Harrison, S.P.: *smpds*: The SPECIAL Modern Pollen Data Set for Climate Reconstructions
668 (v2.0.0). Zenodo. <https://doi.org/10.5281/ZENODO.6598832>, 2022. (last accessed 17 April 2023)
- 669 Villegas-Diaz, R., Cruz-Silva, E., and Harrison, S.P.: *ageR*: Supervised Age Models [R]. Zenodo.
670 <https://doi.org/10.5281/zenodo.4636716>, 2021 (last accessed 17 April 2023).
- 671 Villegas-Diaz, R., Prentice, I.C., and Harrison, S.P.: *COdos*: CO₂ Correction Tools [R]. SPECIAL Research Group.
672 <https://github.com/special-uor/codos>, 2022. (last accessed 17 April 2023)
- 673 Wei, D., González-Sampériz, P., Gil-Romera, G., Harrison, S.P., and Prentice, I.C.: Seasonal temperature and
674 moisture changes in interior semi-arid Spain from the last interglacial to the Late Holocene, *Quat. Res.*, 101,
675 143–155. <https://doi.org/10.1017/qua.2020.108>, 2021.
- 676 Weiberg, E., Bevan, A., Kouli, K., Katsianis, M., Woodbridge, J., Bonnier, A., Engel, M., Finné, M., Fyfe, R.,
677 Maniatis, Y., Palmisano, A., Panajiotidis, S., Roberts, C. N., and Shennan, S.: Long-term trends of land use and
678 demography in Greece: A comparative study, *Holocene*, 29, 742–760,
679 <https://doi.org/10.1177/0959683619826641>, 2019.
- 680 Weninger, B., Alram-Stern, E., Bauer, E., Clare, L., Danzeglocke, U., Jöris, O., Kubatzki, C., Rollefson, G.,
681 Todorova, H., and van Andel, T.: Climate forcing due to the 8200 cal yr BP event observed at Early Neolithic
682 sites in the eastern Mediterranean, *Quat. Res.*, 66, 401–420, <https://doi.org/10.1016/j.yqres.2006.06.009>,
683 2006.
- 684
- 685 Yanchilina, A.G., Ryan, W.B.F., Kenna, T.C., and McManus, J.F.: Meltwater floods into the Black and Caspian
686 Seas during Heinrich Stadial 1, *Earth Sci. Rev.*, 198, 102931, <https://doi.org/10.1016/j.earscirev.2019.102931>,
687 2019.
- 688
- 689 Zeder, M.A.: The origins of agriculture in the Near East, *Curr. Anthropol.*, 52), S221–S235,
690 <https://doi.org/10.1086/659307>, 2011.
- 691 Zhang, Y., Renssen, H., and Seppä, H.: Effects of melting ice sheets and orbital forcing on the early Holocene
692 warming in the extratropical Northern Hemisphere, *Clim. Past*, 12, 1119–1135. <https://doi.org/10.5194/cp-12-1119-2016>, 2016.
- 693
- 694 Zhang, Y., Renssen, H., Seppä, H., and Valdes, P. J.: Holocene temperature trends in the extratropical
695 Northern Hemisphere based on inter-model comparisons, *J. Quat. Sci.*, 33, 464–476.
696 <https://doi.org/10.1002/jqs.3027>, 2018.



697 **Figure and Table Captions**

698 Figure 1. Distribution of pollen records used in the climate reconstructions. The colour coding shows the length
699 of the record.

700 Figure 2. Time series of reconstructed anomalies of mean temperature of the coldest month (MTCO) for
701 individual records. Entities are arranged by latitude (N-S). Information about the numbered individual sites
702 can be found in Supplementary Table 1.

703 Figure 3. Time series of reconstructed anomalies of mean temperature of the warmest month (MTWA) for
704 individual records. Entities are arranged by latitude (N-S). Information about the numbered individual sites
705 can be found in Supplementary Table 1.

706 Figure 4. Time series of reconstructed anomalies of plant available moisture, expressed as the ratio between
707 potential and actual evapotranspiration (α), at individual sites. A correction to account for the direct
708 physiological impacts of CO₂ on plant growth has been applied to the reconstructed α . Entities are arranged
709 by latitude (N-S). Information about the numbered individual sites can be found in Supplementary Table 1.

710 Figure 5. Composite changes in reconstructed mean temperature of the coldest month (MTCO), mean
711 temperature of the warmest month (MTWA), growing degree days above a base level of 0°C (GDD0), and plant
712 available moisture expressed as the ratio between potential and actual evapotranspiration (α). A correction
713 to account for the direct physiological impacts of CO₂ on plant growth has been applied to the reconstructions
714 of α . The green line is a loess smoothed curve through the reconstruction with a window half width of 500
715 years; the green shading shows the uncertainties based on 1000 bootstrap resampling of the records. The
716 bottom panel shows the number of records used to create the composite through time.

717 Figure 6. Simulated regional changes in mean temperature of the coldest month (MTCO), mean temperature
718 of the warmest month (MTWA), growing degree days above a base level of 0°C (GDD0), and plant available
719 moisture expressed as the ratio between potential and actual evapotranspiration (α) in the EMBSecBIO
720 domain from the TRACE-21K-I (green) and TRACE-21K-II (red) transient simulations. It is not possible to
721 calculate changes in α for the TRACE-21K-II simulation from the available data. Loess smoothed curves were
722 drawn using a window half width of 500 years, and the envelope was obtained through 1000 bootstrap
723 resampling of the sequences. The top panel shows the changes in summer and winter insolation (Wm⁻²) at 40°
724 N.

725 Figure 7. Simulated regional changes in mean temperature of the coldest month (MTCO), mean temperature
726 of the warmest month (MTWA), and growing degree days above a base level of 0°C (GDD0) in the EMBSecBIO
727 domain from the LOVECLIM transient simulation. It is not possible to calculate changes in α for the LOVECLIM
728 simulation from the available data. Loess smoothed curves were drawn using a window half width of 500
729 years, and the envelope was obtained through 1000 bootstrap resampling of the sequences.

730 Figure 8. Simulated regional changes in mean temperature of the coldest month (MTCO), mean temperature
731 of the warmest month (MTWA), and growing degree days above a base level of 0°C (GDD0) in the EMBSecBIO
732 domain from the four PACMEDY simulations. The models are: Max Plank Institute Earth System Model (MPI),
733 Alfred Wegener Institute Earth System Model simulations (AWI), Institute Pierre Simon Laplace Climate Model
734 TR5AS simulation (IPSL-CM5) and Institute Pierre Simon Laplace Climate Model TR6A V simulation (IPSL-CM6).
735 Loess smoothed curves were drawn using a window half width of 500 years and the envelope was obtained
736 through 1000 bootstrap resampling of the sequences.



737 Figure 9. Comparison of regional composites of reconstructed seasonal temperatures from this study with
738 those derived from Mauri et al. (2015) and Herzschuh et al. (2022). Mauri et al. (2015 provide mean
739 temperature of the coldest month (MTCO) and mean temperature of the warmest month (MTWA)
740 reconstructions, which can be directly compared with our reconstructions. Herzschuh et al. (2022) only
741 provide reconstructions of July temperature. Our reconstructions are shown in blue, reconstructions based on
742 the Mauri et al. (2015) data set are shown in green, and reconstructions based on the Herzschuh et al.
743 reconstruction are shown in orange. The solid line is a loess smoothed curve through the reconstruction with
744 a window half width of 500 years; the shading shows the uncertainties based on 1000 bootstrap resampling
745 of the records.

746 Table 1. Leave-out cross-validation fitness of fXTWA-PLSv2 for mean temperature of the coldest month
747 (MTCO), mean temperature of the warmest month (MTWA), growing degree days above base level 0°C (GDD0)
748 and plant-available moisture (α) with p-spline smoothed fx estimation, using bins of 0.02, 0.02 and 0.002,
749 showing results for the selected component for each variable. RMSEP is the root-mean-square error of
750 prediction. p assesses whether using the current number of components is significantly different from using
751 one component less. The degree of overall compression is assessed by linear regression of the cross-validated
752 reconstructions onto the climate variable, where b1 and b1.se are the slope and the standard error of the
753 slope, respectively. The overall compression is reduced as the slope approaches 1. Full details for all the
754 components are given in Supplementary Table 4.

755

756

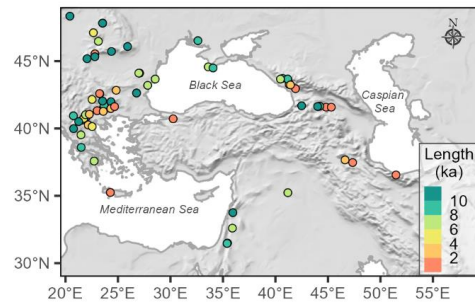
757

758

759



760 Figure 1. Distribution of pollen records used in the climate reconstructions. The colour coding shows the
761 length of the record.



762

763

764

765

766

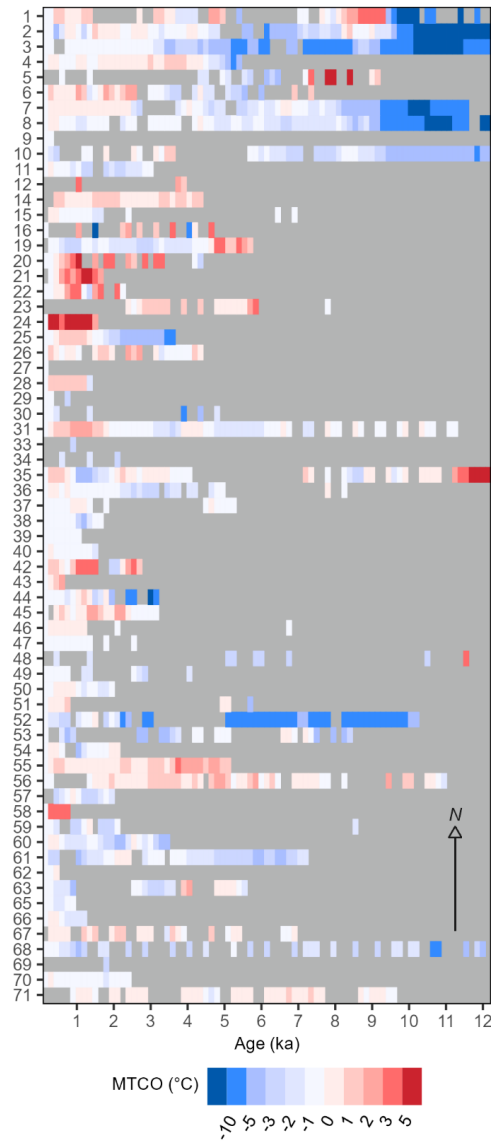
767

768

769



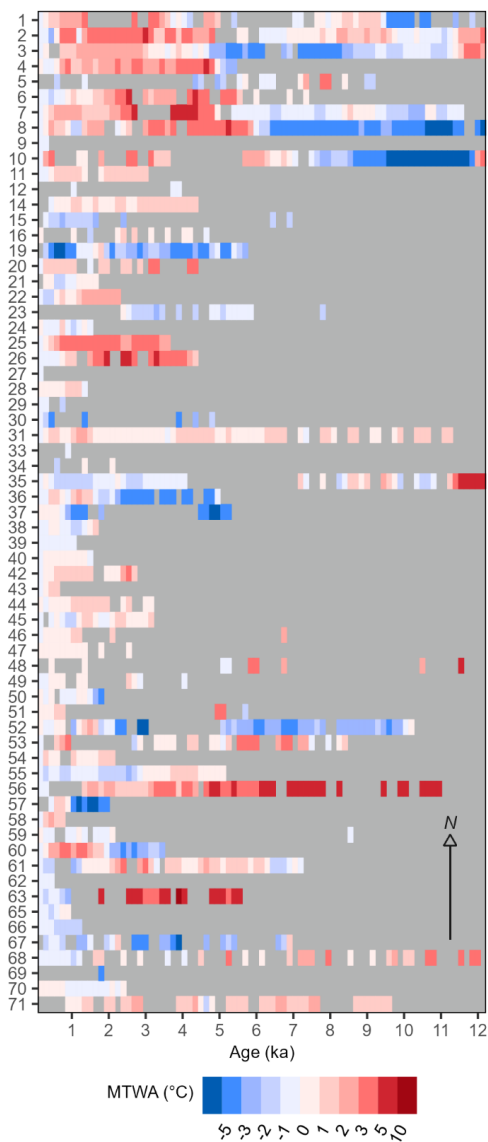
770 Figure 2. Time series of reconstructed anomalies of mean temperature of the coldest month (MTCO) for
771 individual records. Entities are arranged by latitude (N-S). Information about the numbered individual sites
772 can be found in Supplementary Table 1.



773
774
775
776
777



778 Figure 3. Time series of reconstructed anomalies of mean temperature of the warmest month (MTWA) for
779 individual records. Entities are arranged by latitude (N-S). Information about the numbered individual sites
780 can be found in Supplementary Table 1.



781

782

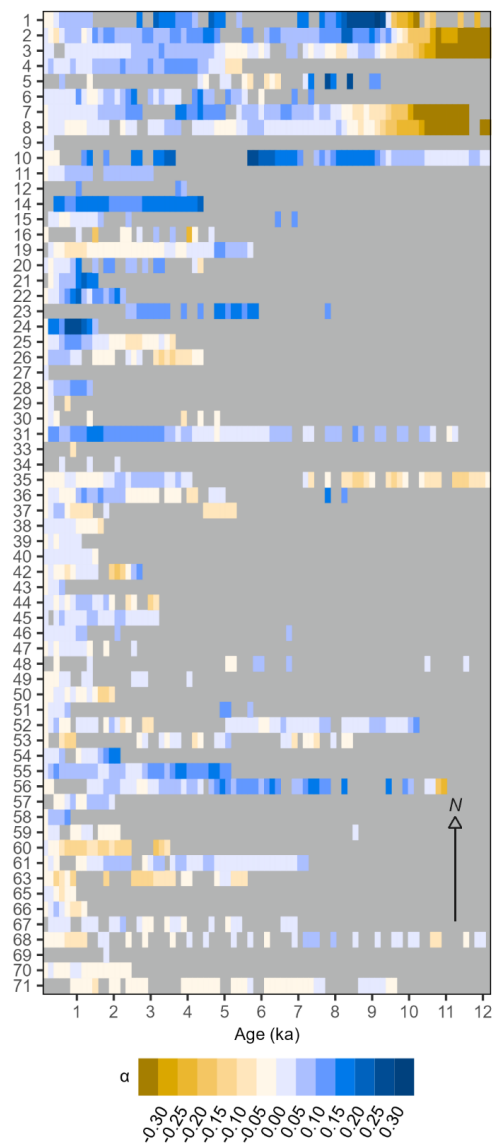
783

784



785 Figure 4. Time series of reconstructed anomalies of plant available moisture, expressed as the ratio between
786 potential and actual evapotranspiration (α), at individual sites. A correction to account for the direct
787 physiological impacts of CO₂ on plant growth has been applied to the reconstructed α . Entities are arranged
788 by latitude (N-S). Information about the numbered individual sites can be found in Supplementary Table 1.

789

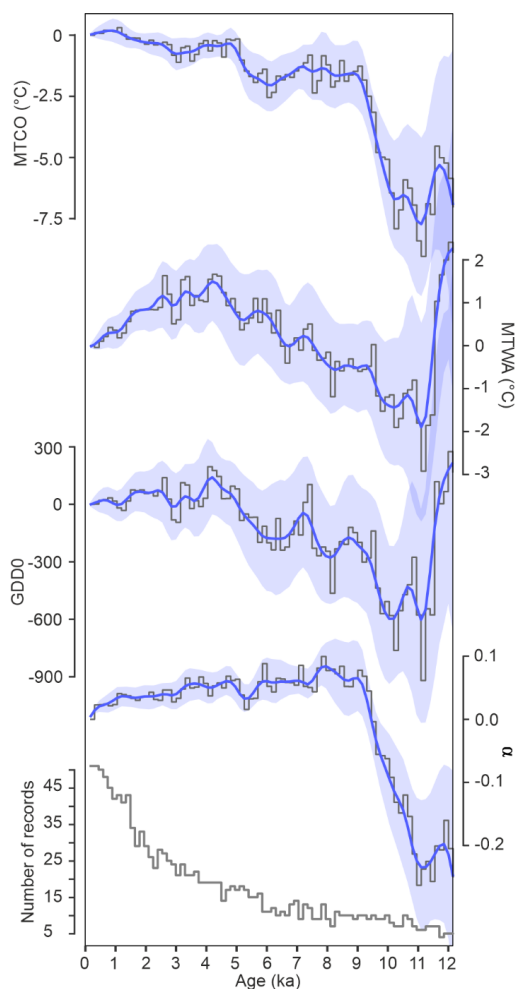


790

791



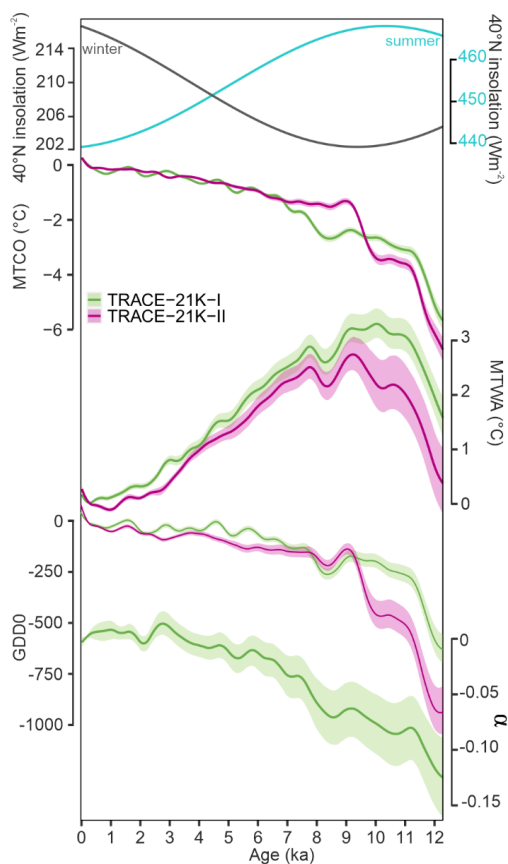
792 Figure 5. Composite changes in reconstructed mean temperature of the coldest month (MTCO), mean
793 temperature of the warmest month (MTWA), growing degree days above a base level of 0°C (GDD0), and
794 plant available moisture expressed as the ratio between potential and actual evapotranspiration (α). A
795 correction to account for the direct physiological impacts of CO₂ on plant growth has been applied to the
796 reconstructions of α . The green line is a loess smoothed curve through the reconstruction with a window
797 half width of 500 years; the blue shading shows the uncertainties based on 1000 bootstrap resampling of the
798 records. The bottom panel shows the number of records used to create the composite through time.



799
800
801
802
803
804



805 Figure 6. Simulated regional changes in mean temperature of the coldest month (MTCO), mean temperature
806 of the warmest month (MTWA), growing degree days above a base level of 0°C (GDD0), and plant available
807 moisture expressed as the ratio between potential and actual evapotranspiration (α) in the EMBSeCBIO
808 domain from the TRACE-21K-I (green) and TRACE-21K-II (red) transient simulations. It is not possible to
809 calculate changes in α for the TRACE-21K-II simulation from the available data. Loess smoothed curves were
810 drawn using a window half width of 500 years, and the envelope was obtained through 1000 bootstrap
811 resampling of the sequences. The top panel shows the changes in summer and winter insolation (Wm^{-2}) at 40°
812 N.



813

814

815

816

817

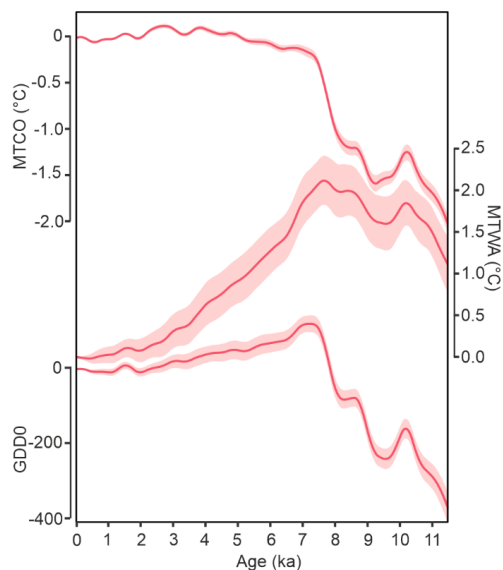
818

819

820



821 Figure 7. Simulated regional changes in mean temperature of the coldest month (MTCO), mean temperature
822 of the warmest month (MTWA), and growing degree days above a base level of 0°C (GDD0) in the EMBSecBIO
823 domain from the LOVECLIM transient simulation. It is not possible to calculate changes in α for the LOVECLIM
824 simulation from the available data. Loess smoothed curves were drawn using a window half width of 500
825 years, and the envelope was obtained through 1000 bootstrap resampling of the sequences.



826

827

828

829

830

831

832

833

834

835

836

837

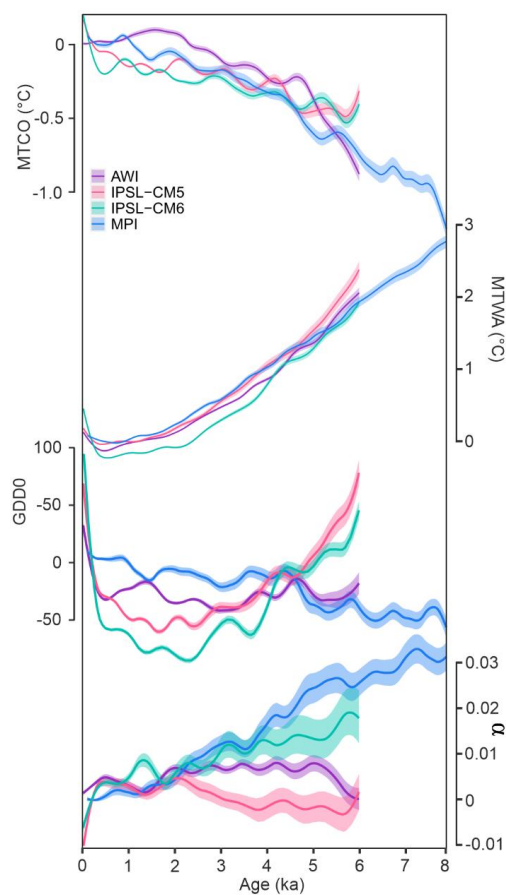
838

839

840



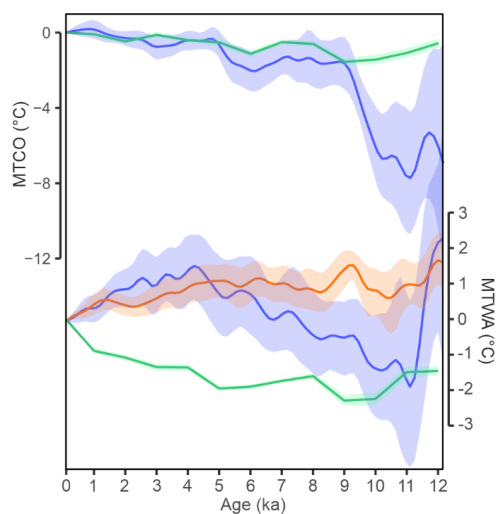
841 Figure 8. Simulated regional changes in mean temperature of the coldest month (MTCO), mean temperature
842 of the warmest month (MTWA), and growing degree days above a base level of 0°C (GDD0) in the
843 EMBSeCBIO domain from the four PACMEDY simulations. The models are: Max Plank Institute Earth System
844 Model (MPI), Alfred Wagener Institute Earth System Model simulations (AWI), Institute Pierre Simon Laplace
845 Climate Model TR5AS simulation (IPSL-CM5) and Institute Pierre Simon Laplace Climate Model TR6A V
846 simulation (IPSL-CM6). Loess smoothed curves were drawn using a window half width of 500 years and the
847 envelope was obtained through 1000 bootstrap resampling of the sequences.



848
849
850
851
852
853
854
855



856 Figure 9. Comparison of regional composites of reconstructed seasonal temperatures from this study with
857 those derived from Mauri et al. (2015) and Herzschuh et al. (2022). Mauri et al. (2015 provide mean
858 temperature of the coldest month (MTCO) and mean temperature of the warmest month (MTWA)
859 reconstructions, which can be directly compared with our reconstructions. Herzschuh et al. (2022)
860 only provide reconstructions of July temperature. Our reconstructions are shown in blue, reconstructions based on
861 the Mauri et al. (2015) data set are shown in green, and reconstructions based on the Herzschuh et al.
862 reconstruction are shown in orange. The solid line is a loess smoothed curve through the reconstruction with
863 a window half width of 500 years; the shading shows the uncertainties based on 1000 bootstrap resampling
864 of the records.



865

866

867



868 **Table 1.** Leave-out cross-validation fitness of fxTWA-PLSv2 for mean temperature of the coldest month
 869 (MTCO), mean temperature of the warmest month (MTWA), growing degree days above base level 0°C (GDD0)
 870 and plant-available moisture (α) with p-spline smoothed fx estimation, using bins of 0.02, 0.02 and 0.002,
 871 showing results for the selected component for each variable. RMSEP is the root-mean-square error of
 872 prediction. p assesses whether using the current number of components is significantly different from using
 873 one component less. The degree of overall compression is assessed by linear regression of the cross-validated
 874 reconstructions onto the climate variable, where b1 and b1.se are the slope and the standard error of the
 875 slope, respectively. The overall compression is reduced as the slope approaches 1. Full details for all the
 876 components are given in Supplementary Table 4.

Variable	Selected component	R2	Average bias	RMSEP	p	b1	b1.se
MTCO	4	0.73	-0.22	3.67	0.001	0.86	0.01
MTWA	2	0.63	-0.10	3.22	0.001	0.78	0.01
GDD0	2	0.69	56.46	880.33	0.001	0.79	0.01
α	2	0.73	-0.01	0.15	0.001	0.80	0.01

877

878

879

880

881

882

883

884

885

886

887